Inorganic Chemistry

pubs.acs.org/IC

Article

Role of Coordination Geometry on the Magnetic Relaxation Dynamics of Isomeric Five-Coordinate Low-Spin Co(II) Complexes

Lena Spillecke,*[,⊥] Shalini Tripathi,[⊥] Changhyun Koo, Arne Bahr, Abinash Swain, Rajashi Haldar, Mursaleem Ansari, Jerry Jasinski, Gopalan Rajaraman,* Maheswaran Shanmugam,* and Rüdiger Klingeler*

Cite This: *Inorg. Chem.* 2022, 61, 317−327

Read Online

ACCESS | Metrics & More | Article Recommendations | Supporting Information

ABSTRACT: To investigate the influence of the coordination geometry on the magnetization relaxation dynamics, two geometric isomers of a five-coordinate low-spin Co(II) complex with the general molecular formula $[Co(DPPE)_2Cl]SnCl_3$ (DPPE = diphenylphosphinoethane) were synthesized and structurally characterized. While one isomer has a square pyramidal geometry (Co-SP (**1**)), the other isomer figures a trigonal bipyramidal geometry (Co-TBP (**2**)). Both complexes were already reported elsewhere. The spin state of these complexes is unambiguously determined by detailed direct current (dc) magnetic data, X-band, and high-frequency EPR measurements. Slow relaxation of magnetization is commonly observed for systems with $S > 1/2$. However, both **1** and **2** show field-induced slow relaxation of magnetization. Especially **1** shows relaxation times up to $\tau = 35$ ms at $T = 1.8$ K, which is much longer than the reported values for undiluted Co(II) low-spin monomers. In **2**, the maximal field-induced relaxation time is suppressed to $\tau = 5$ ms. We attribute this to the change in g-anisotropy, which is, in turn, correlated to the spatial arrangement of ligands (i.e., coordination geometry) around the Co(II) ions. Besides the detailed electronic structure of these complexes, the experimental observations are further corroborated by theoretical calculations.

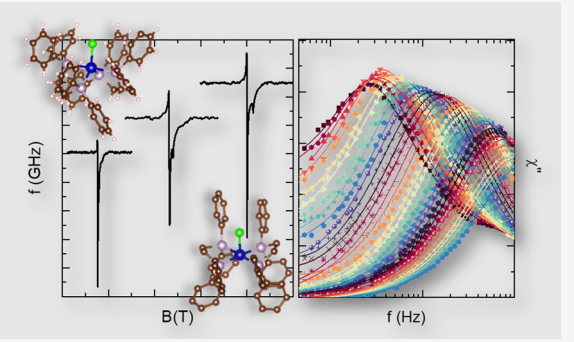

INTRODUCTION

Finding applicable quantum systems to build efficient spin qubits, i.e., systems which figure a reasonable relaxation time to store information, on the one hand, but can be easily and quickly manipulated, on the other hand, is one of the main prerequisites for nowadays development of quantum computing and quantum processing devices.[1−4] It is the zero-field energy gap or the magnetic anisotropy which is often recalled as a key characteristic of this material class so that a large variety of research mainly focuses on either its tuning or enhancement.[5−13] Specifically, a high anisotropy barrier can strongly enhance the longitudinal relaxation time T_1 which describes the lifetime of a classical bit with two reachable states. For an entangled quantum state, the limiting factor is the transversal relaxation time T_2 which measures the phase memory time of a superposition state.[4,14] Although systems with a spin $S = 1/2$ do not feature an anisotropy barrier, they naturally provide long transversal relaxation times up to high temperatures owing to the absence of excited energy levels which could promote relaxation processes.[4,15] However, due to the presence of spin−spin and hyperfine interactions, the field-induced slow relaxation of magnetization behavior is often suppressed in undiluted systems which is why examples are rather scarce in the literature.[4,16−21] Especially in the case of an undiluted Co(II) low-spin (LS) monomeric complex, there is only a limited amount of examples reported so far.[19,22,23]

It is proposed that the spatial distribution of the ligands around the central metal ion is a crucial parameter influencing the relaxation behavior of a spin $S = 1/2$.[16,24] However, no example of investigations of the longitudinal relaxation time on systems that are real geometrical isomers can be found in the literature. The lack of such investigation is presumably linked to the isolation of isomers using the same ligands employed, i.e., only the thermodynamically stable coordination geometry crystallizes, while the other one does not. Overcoming this challenging issue by our synthetic approach, we have isolated both geometric isomers of a five-coordinate Co(II) complex, i.e., square pyramidal (Co-SP (**1**)) and trigonal bipyramidal (Co-TBP (**2**)) coordination geometry, which is structurally characterized by single-crystal X-ray diffraction confirming the general molecular formula of $[Co(DPPE)_2Cl]SnCl_3$ (DPPE =

Received: September 15, 2021
Published: December 17, 2021

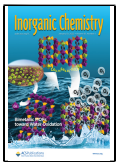

diphenylphosphinoethane). Both complexes were already reported elsewhere.[25−27] Detailed dc magnetization, as well as X-band and high-frequency/high-field electron paramagnetic resonance (HF-EPR) measurements reveal that the g-anisotropy is changing with the spatial orientation of the ligands surrounding the Co(II) center. In addition, the X-band EPR investigations imply a change in hyperfine interaction strength. These parameters' influence is reflected in the magnetization relaxation dynamics of these two complexes. The detailed electronic structure and the distinct changes in the magnetic properties of the complexes are rationalized using theoretical calculations.

EXPERIMENTAL AND METHODS SECTION

Unless otherwise stated, the reactions were carried out under aerobic conditions. All chemicals were purchased from commercially available sources (Alfa Aesar/Sigma-Aldrich). Single-crystal X-ray data collection was done on a Rigaku Saturn CCD diffractometer using a graphite monochromator (λ = 0.71073 Å). The unit cell determination and data reduction was performed using CrysAlisPro 1.171.38.43 (Rigaku OD, 2015). The structures were solved by direct methods and refined by least-squares procedures on F^2 with SHELXL-2014/7.[28] All non-hydrogen atoms were refined anisotropically, and hydrogen atoms were added in their geometrically calculated positions which were refined as a riding model. Elemental analysis was carried out with a Thermo Finnigan device. The powder XRD data (λ = 1.5406 Å) was collected with a Panalytical MRD system (CCDC numbers for **1**: 2080078, **2**: 2080079).

X-band electron paramagnetic resonance (EPR) spectra were recorded using a Bruker EMXPLUS spectrometer. Direct current (dc) as well as dynamic alternating current (ac) magnetization measurements were performed using an MPMS3 SQUID (superconducting quantum interference device) magnetometer (Quantum Design) equipped with a 7 T magnet. Depending on the device and measurement technique, the samples were fixed in gelatin capsules and placed inside a non-magnetic straw sample holder or pressed in a plastic capsule and mounted on a brass sample holder. Temperature-dependent dc measurements were performed in between 1.8 and 300 K with an applied magnetic field of 1 T. For the field-dependent measurements, the external magnetic field was swept up to 7 T at several fixed temperatures. The ac measurements were conducted under applied dc fields of 0, 0.2, and 1 T, respectively, at temperatures ranging from 1.8 to 7 K with an oscillating magnetic field of 3 Oe at frequencies ranging from 1 to 1000 Hz. High-field electron paramagnetic resonance (HF-EPR) measurements were carried out using a phase-sensitive millimeter-wave vector network analyzer (MVNA) from AB Millimeter as a microwave source and detector.[29] Measurements have been performed at frequencies between 50 and 300 GHz and in magnetic fields up to 16 T. Various measurement frequencies were realized by the assembling of Shottky diodes for different bands, e.g. V, W, and D bands. The temperature was controlled by the regulation of ^{4}He gas flow in a variable temperature insert (VTI). The powder samples were fixed by mixing with eicosane inside a brass ring which was placed on the end of a transmission-type tube-shaped probe. Analysis of magnetization and EPR data was done by means of the EasySpin software package.[30]

Density field theory (DFT) calculations have been performed using the Gaussian 09 suite.[31] The geometries were optimized using the B3LYP-D2 functional, incorporating the dispersion correction proposed by Grimme et al.[32] We have used two different basis sets: LanL2DZ, which encompasses a double-ζ quality basis set with the Los Alamos effective core potential for Co, P, and Cl, and a 6-31G* basis set for the other atoms (C and H).[33,34] The quoted DFT energies are B3LYP-D2 energies at a temperature of 298.15 K. The exchange between the neighboring Co(II) ions in the crystal lattice has been calculated using the Broken-Symmetry approach with a B3LYP functional with the TZVP level of the basis for Co and TZV for the rest of the atoms. The quantum chemical calculations were carried out using the ORCA (4.2.1)[35] suite directly on the crystal structures obtained through single-crystal X-ray diffraction. Spin Hamiltonian (SH) parameters were calculated using multireference *ab initio* calculations. State-average complete active space self-consistent field (CASSCF) calculations were performed on both complexes. Scalar relativistic effects are treated using the DKH method.[36,37] The valenced polarized triple-ζ (def2-TZVP) quality basis set along with TZVP/C as an auxiliary basis set for the resolution of identity (RI) approximation for cobalt, phosphorus (def2-TZVP(-f)), and chlorine was used, whereas the def2-SVP quality basis set along with SVP/C as an auxiliary basis set was used for the rest of the atoms.[38,39] The calculations were performed with an active space of CAS (7,5) which corresponds to seven active d-electrons in five active d-orbitals. Followed by CASSCF, NEVPT2 calculations have been performed to recover the dynamic correlations and to predict the correct spin state, from which the g-factors have been derived.[40,41]

Synthesis of [CoCl(DPPE)$_2$]SnCl$_3$ (Co-SP (1)). $CoCl_2{\cdot}6H_2O$ (0.24 g, 1 mmol) was added to the boiling n-butanol (30 mL) in a 250 RB flask at room temperature (RT), which was refluxed for 5 min. After 5 min, $SnCl_2{\cdot}2H_2O$ (0.23 g, 1 mmol) was added, and the reflux was continued for another 5 min. In the following step, the DPPE (1,2-bis(diphenylphosphino)ethane) (0.81 g, 2.0 mmol) ligand was added into the reaction mixture (under reflux conditions). Upon addition of DPPE, the reaction mixture turned olive green. As soon as the DPPE was added to the reaction mixture, the reaction flask was removed from heating and allowed to cool down to room temperature. Upon cooling, orange-red color single crystals began to grow which were suitable for single-crystal X-ray diffraction. Elemental analysis calculated (%): C, 55.95; H, 4.33. Found: C, 55.54; H, 4.27. Infrared (cm^{-1}) = $\nu_{(C-H)}$ = 3053 cm^{-1} (sharp), $\nu_{(C=C)}$ = 1621 cm^{-1} (sharp), $\nu_{(C-H\ bending)}$ = 1482, 1443 cm^{-1} (very sharp) (Figure S1 of the SI).

Synthesis of [CoCl(DPPE)$_2$]SnCl$_3$ (Co-TBP (2)). An exactly similar procedure has been followed as in **1**, but the order of addition was changed; i.e., into the cobalt chloride solution of n-butanol, the DPPE (0.81 g, 2 mmol) ligand was added first, followed by $SnCl_2{\cdot}2H_2O$. In the same way, as found for the reaction in **1**, crystals were beginning to grow upon cooling the reaction mixture. Dark green single crystals with reasonably good yield were obtained which were suitable for single-crystal X-ray diffraction. Elemental analysis calculated (%): C, 55.95; H, 4.33. Found: C, 55.77; H, 4.31. Infrared (cm^{-1}) = $\nu_{(C-H)}$ = 3053 (sharp), $\nu_{(C=C)}$ = 1621 (sharp), $\nu_{(C-H\ bending)}$ = 1482, 1443 (very sharp) (Figure S1 of the SI).

The powder X-ray diffraction (PXRD) features of **1** and **2** measured at room temperature are in good agreement with the XRD pattern generated from their corresponding single-crystal X-ray diffraction, which confirms the bulk phase purity of complexes **1** and **2** (Figure S2 of the SI).

RESULTS AND DISCUSSION

Structural Analysis. The reaction of cobalt chloride in the presence of DPPE (1,2-bis(diphenylphosphino)ethane) and stannous chloride hydrate in n-butanol led us to isolate two different geometric isomers of the Co(II) complex which are in a different color, i.e., orange-red (Co-SP; **1**) and dark green (Co-TBP; **2**) (cf. Scheme 1). Isolation of these two isomers, exclusively controlled by the order of addition of the precursors (see the Experimental and Methods Section for details), is distinctly different from the other synthetic procedures reported in the literature.[25−27]

Data collection and structure solution reveal the general molecular formula in both cases as [Co(DPPE)$_2$Cl](SnCl$_3$), but the Co(II) complex in orange-red and dark green colored crystals was found to be in a square pyramidal (hereafter called Co-SP (**1**)) and trigonal bipyramidal (hereafter called Co-TBP (**2**)) coordination geometry, respectively. Both complexes possess the same molecular formula, but they do differ in their

https://doi.org/10.1021/acs.inorgchem.1c02881
Inorg. Chem. 2022, 61, 317−327

Scheme 1. General Synthetic Procedure Which Was Followed to Isolate Complexes 1 and 2

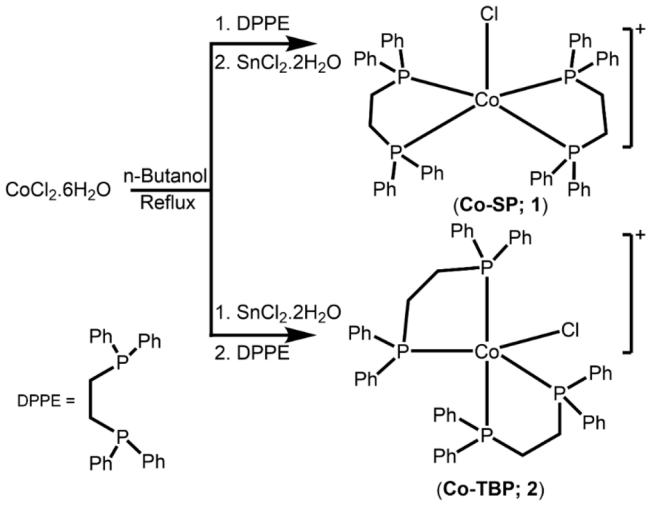

coordination geometry. Hence, they are geometrical isomers as well as structural polymorphs. The oxidation state and the coordination geometry around the Co(II) ion in **1** and **2** were confirmed by bond valence sum (BVS) calculations[42] and Continuous Shape Measurement (CShM) analysis, respectively (Figure 1 and Table S1 of the SI).[43] To confirm further the geometry around the Co(II) ion in **1** and **2**, the structural index parameter (τ) was calculated, which is described in detail elsewhere.[44] A τ-value of 0 and 1 represents an ideal square pyramidal and trigonal bipyramidal coordination geometry around the metal ion, respectively. Deviations from these values denote the extent of distortion from their ideal coordination geometry. The τ-parameter calculated for **1** and **2** was observed to be 0.08 and 0.91, respectively. This not only confirms the coordination predicted by CShM but also implies that there is a slight distortion observed in the respective geometry in both complexes.

We would like to point out that the crystal structure of these complexes is reported elsewhere,[27] but the authors claimed that the two different geometric isomers of the five-coordinate Co(II) ions are accessible by changing the solvent. However, under the reported conditions, we were unable to isolate the complexes in the way which was described. A detailed investigation led us to conclude that the order of the addition of reagents to the cobalt chloride solution is more important (in butanol solution) than changing the solvent.

Due to the change in the reaction conditions, the unit cell and the crystal system observed for **1** and **2** were slightly different from the structure reported elsewhere.[25] Therefore, the crystal data was recollected and solved again. The coordinates obtained from these data were used for the DFT calculations (*vide infra*). Furthermore, we would like to note that based on the preliminary magnetic and ^{119}Sn Mössbauer measurements on the polymorphs of **1** and **2** reported elsewhere, we find that the Co(II) ions are in a low-spin state, i.e., $S = 1/2$.[25−27] However, no detailed magnetic studies have been reported so far for these complexes, e.g., field-induced slow relaxation of magnetization.

The single-crystal data collection and structure solution of **1** and **2** reveal that these complexes crystallize in the monoclinic, $P2_1/n$ and triclinic, P-1 space groups (Table 1), respectively. In both complexes, two bidentate DPPE and a halide ion complete the coordination sites around the Co(II) ion. In **2**, the axial position is occupied by two phosphorus ligands of DPPE, while the equatorial positions are completed by two phosphorus atoms and a chloride ion. The average Co−P (axial) and Co−P (equatorial) distance is found to be 2.261(1) Å and 2.275(1) Å, respectively, while the Co−Cl bond distance is observed to be 2.274(2) Å. The bond angle

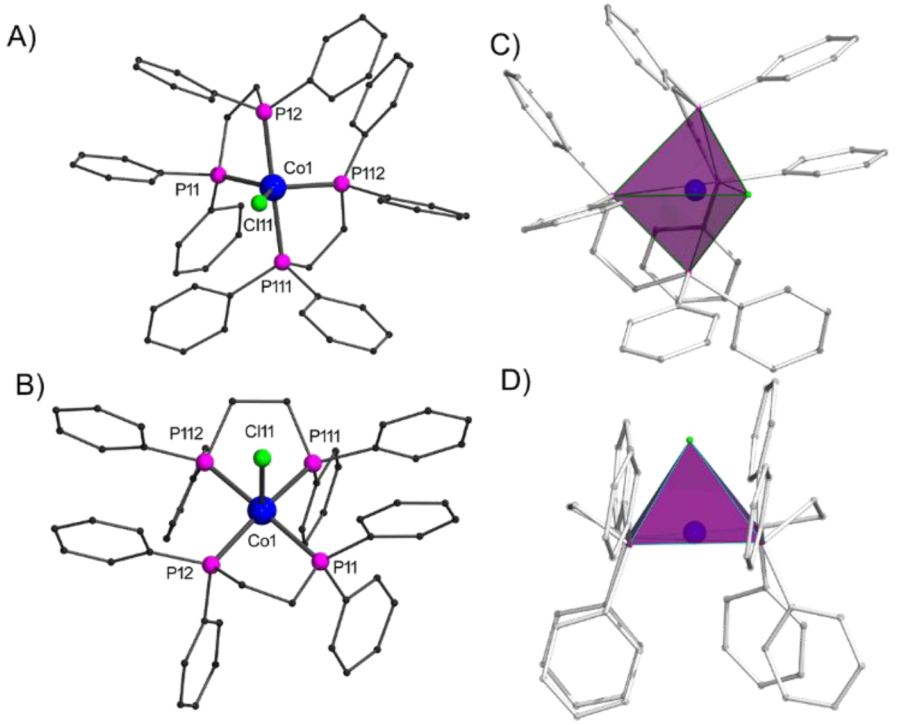

Figure 1. Crystal structure for complexes **2** (A) and **1** (B). (C) and (D) panels represent the polyhedral view for **2** and **1**, respectively.

https://doi.org/10.1021/acs.inorgchem.1c02881
Inorg. Chem. 2022, 61, 317−327

Table 1. Crystallographic Parameters for Complexes 1 and 2

	Co-SP; 1	Co-TBP; 2
empirical formula	$C_{52}H_{48}Cl_4CoP_4Sn$	$C_{52}H_{48}Cl_4CoP_4Sn$
crystal system	monoclinic	triclinic
space group	$P2_1/n$	$P\text{-}1$
a (Å)	17.5352(13)	11.9814(5)
b (Å)	16.340(1)	12.8232(6)
c (Å)	18.1518(15)	17.5456(8)
α [deg]	90	104.104(4)
β [deg]	113.371(10)	90.225(4)
γ [deg]	90	107.888(4)
V [Å^3]	4774.3(7)	2479.0(2)
Z	4	2
T (K)	150	150
ρ_{calcd} [g cm^{-3}]	1.553	1.495
$2\theta_{max}$	50.00	49.996
radiation	Mo K_α	Mo K_α
λ [Å]	0.71073	0.71073
no. of reflections	32083	39203
no. of indep reflections	8409	8740
no. of reflections with $I > 2\sigma(I)$	5079	6303
R_1	0.0651	0.0742
wR_2	0.1290	0.2027

∠P12−Co1−P111 (176.06(8)°) of the axially coordinated atoms slightly deviates from a perfect linear structure by 4°. Considerable distortion is observed in the equatorial bond angles, i.e., ∠P11−Co1−P112, ∠P11−Co1−Cl11, and ∠P112−Co1−Cl11, which are found to be 107.9(3)°, 124.9(2)°, and 127.2(2)°, respectively.

The presence of a chloride point charge ligand bound to the Co(II) ion leads to an overall positive charge on the coordination sphere of the Co(II) ion. To neutralize this cationic charge, an $SnCl_3^-$ anion resides in the crystal lattice of **2**. The divalent tin ion surrounded by three chloride ions exhibits a pyramidal coordination geometry. The average Sn−Cl bond length is found to be 2.465(2) Å, while the average ∠Cl−Sn−Cl bond angle is 93.83(8)°. The structural parameters observed in **2** are consistent with the ones for the polymorph Co-TBP complex reported elsewhere.[25−27] Selected bond lengths and bond angles corresponding to the structure of **2** are given in Table S2. The closest Co···Sn distance is found to be 7.769(3) Å. Although **2** is, in general, structurally similar to the reported complex, a slight deviation from the reported parameters is observed.

The crystal structures of **1** and **2** were analyzed carefully and revealed that there are no classical H-bondings in these complexes, but a signature of extremely weak inter- and intramolecular interactions spread across all directions. In **2**, it seems that the halide ions bound to the Sn(II) are involved in a weak intermolecular interaction with aromatic protons (C19···Cl 1 = 3.658(7) Å, C19···Cl 2 = 3.781(7) Å, C122···Cl 3 = 3.620(8) Å) and aliphatic protons (C4···Cl 2 = 3.754(7) Å, C4···Cl 3 = 3.780(8) Å) of the phenyl group at the DPPE ligand. Besides, in **1**, the halide ion bound to the Co(II) ion (Cl 11) is involved in a weak intramolecular interaction with aromatic protons of the DPPE ligand (C24···Cl 1 = 3.668(8) Å and C12···Cl 2 = 3.620(9) Å, C116···Cl 11 = 3.611(6) Å, and C16···Cl 11 = 3.668(7) Å). The existence of weak intermolecular interactions in both complexes is further investigated by theoretical calculations (*vide infra*).

In contrast to **2**, the basal plane of Co(II) in **1** is completed by two DPPE ligands, and the apical position is occupied by a chloride ion (see Figures 1B and 1D). The average Co−P and Co−Cl bond lengths in **1** were observed to be 2.275(7) Å and 2.403(17) Å, respectively. The Co−P bond distance in **1** and **2** is observed to be similar, however, the Co−Cl bond is significantly longer in **1** (Co1−Cl11 = 2.403(17) Å) than in **2** (Co1−Cl11 = 2.274(2) Å).

Like in **2**, **1** also contains an $SnCl_3^-$ anion in the crystal lattice to compensate for the additional cationic charge on the coordination sphere of the Co(II) ion. The structural parameters of the $SnCl_3^-$ anion in **1** are similar to the bonding parameters observed in complex **2**. The halide atoms coordinated to the Sn(II) and Co(II) ions of both complexes (Cl11 in **1** and **2**) are involved in both inter- and intramolecular weak interactions (Figures S3 and S4 of the SI). The details of the atoms involved in these interactions are listed in Tables S3 and S4 of the SI for **1** and **2**, respectively.

Static Magnetic Properties. Temperature-dependent direct current (dc) magnetic susceptibility measurements performed in a range between 1.8 and 300 K on polycrystalline fixed powder samples of **1** and **2** in the presence of an external magnetic field of B = 1 T are shown in Figures 3(a) and (b), respectively. For both samples, the χ_MT-value figures a

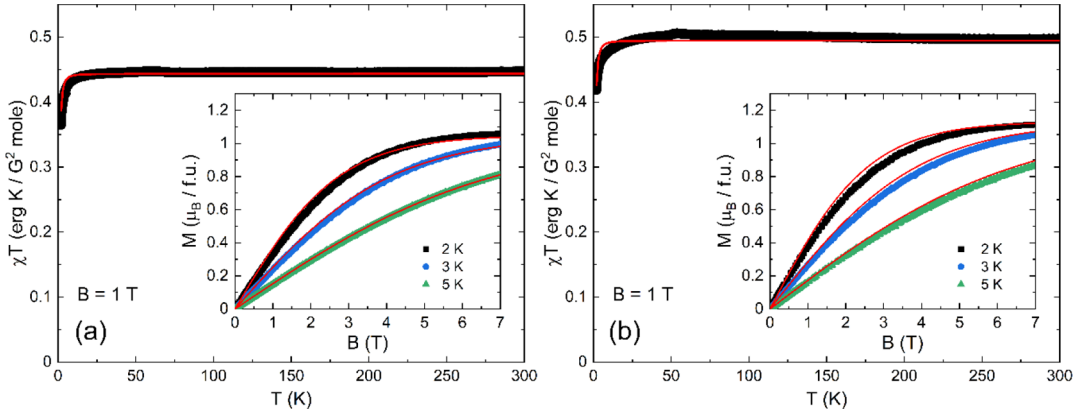

Figure 2. Temperature dependence of the dc susceptibility for **1** (a) and **2** (b) measured in an external magnetic field of B = 1 T. Inset: dc magnetization for **1** and **2** vs external magnetic field at various temperatures. Red solid lines in all plots show a simulation using the g-value obtained from the X-EPR measurements considering a scaling factor of 0.96 and 1.06 for **1** and **2**, respectively, to account for the error in the sample weight.

https://doi.org/10.1021/acs.inorgchem.1c02881
Inorg. Chem. 2022, 61, 317−327

constant behavior in a temperature range between 25 and 300 K. This constant $\chi_M T$ value of 0.44 cm^3 K mol^{-1} and 0.5 cm^3 K mol^{-1} corresponds to an isolated Co(II) low-spin doublet ground state (S = 1/2) with the average g-value of g_{av} = 2.19(5) and 2.33(5), for **1** and **2**, respectively.

The field-dependent magnetization measurements on **1** and **2** are shown as an inset in Figures 2(a) and (b), respectively, for an external magnetic field range between 0 and 7 T at various isothermal conditions (T = 2, 3, and 5 K). Consistent with the low-spin ground state associated with the Co(II) ions in both complexes (**1** and **2**), the magnetic moment tends to saturate around 1.0 μ_B/f.u. and 1.1 μ_B/f.u. at 2.0 K, respectively. Solid red lines in Figure 2 show a simulation using the following spin Hamiltonian (SH)

$$\hat{H} = g\mu_B \vec{S}\cdot\vec{B} \quad (1)$$

with the Bohr magneton μ_B, spin $\vec{S}$, external magnetic field $\vec{B}$, and the g-values obtained from the X-EPR measurements which are shown in the following section. To account for small deviations between the simulation and the magnetization data induced by the error bars of mass determination, a scaling factor of 0.96 and 1.06 had to be introduced for **1** and **2**, respectively, to find the optimal consistency between the measured data and the simulation. Both, the temperature and magnetic field dependence of the magnetic susceptibility are well explained by this model over the whole measurement range. The inverse magnetic susceptibility (χ_M^{-1}) shown in Figures S5(a) and (b) for **1** and **2**, respectively, can be fitted by a Curie law (see red dashed lines in Figures S5(a) and (b)), i.e., the Weiss temperature in a Curie−Weiss approximation is zero within error bars, and thus, no intermolecular interactions are detected on the observed energy scale.

The obtained g-values for **1** and **2** are consistent with the ones reported for other low-spin Co(II) complexes with a planar or square pyramidal coordination geometry.[45−47] Furthermore, we find that the averaged g-value for each complex is larger than the spin-only value of 2.0023 which implies a nonzero contribution of spin−orbit coupling (SOC) and is, thus, in line with the anisotropic g-value of the ground spin doublet state as it is observed in the EPR investigations described in the following section.

X-Band and HF-EPR Measurements. X-band EPR spectra shown in Figure 3 on solid samples confirm the S = 1/2 ground state and display well-resolved resonance lines not only providing information on the anisotropy of the g-factors but also giving evidence for the presence of finite hyperfine interactions between the electronic and the nuclear spin I = 7/2 of the Co(II) ions. In Figure 3(a), it is shown that for **1** three well-resolved resonance features are distinguished which correspond to the three main axes of the g-factor. Due to the broader line width in **2**, the resonance features are not as well resolved as for **1**. However, at least two different signal positions can be read off by eye from the measured data shown in Figure 3(b). The spectra for both samples figure an anisotropic line broadening, which we attribute to unresolved hyperfine interactions with the nuclear moment I = 7/2 of the Co(II) ions.[48] To account for this, we introduced the so-called H-strain parameter which describes an anisotropic residual line width.[30]

However, we would like to mention that anisotropic line broadening can also arise from the g-strain, i.e., from a distribution of the g-principal values induced by intermolecular

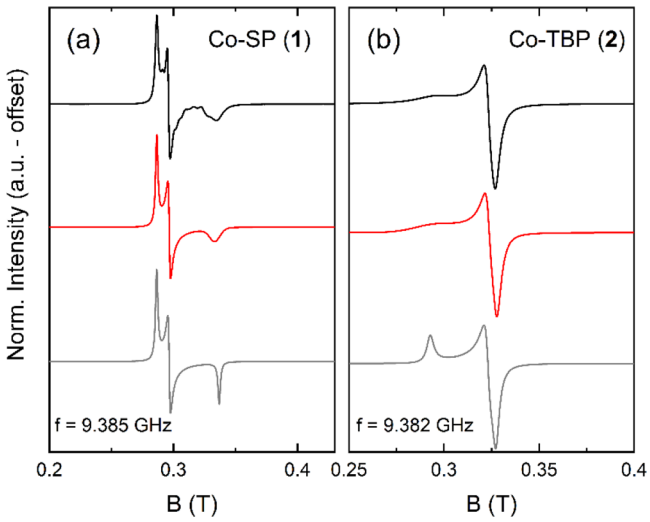

Figure 3. X-band EPR spectra measured at T = 5 K for a fixed powder sample of **1** (a) at f = 9.385 GHz and **2** (b) at f = 9.382 GHz shown as black solid lines. Red solid lines correspond to a simulation including an anisotropic g-factor as well as the line width ω, hyperfine splitting (HFS), and H-strain shown in Table 2 for **1** and **2**, respectively. In order to illustrate the influence of a finite H-strain parameter, an additional simulation without anisotropic line broadening is given as gray lines.

interactions. To investigate this point in more detail, we recorded X-band EPR spectra for both **1** and **2** in a dichloromethane (DCM) solution at 5.0 K (see Figure S6). Upon dissolution of the orange-red crystals of **1** in DCM, the solution turns green, and the frozen solution EPR spectra are distinctly different from the ones obtained for the solid powder but almost perfectly resemble the EPR spectra which were recorded for complex **2** (compare Figures S6 and S8). Hence, we conclude that complex **1** converts into **2** upon dissolution in DCM and can thereby not be investigated in its dissolved form. This conclusion is further corroborated by the UV−vis spectrum recorded for **1** in DCM which shows an absorption profile similar to that observed for **2** in DCM (see Figure S7). Complex **2** shows two intense bands at 318 and 265 nm which are attributed to the charge transfer transitions. A weak band centered at 435 nm and another unresolved one spanning the range between 600 and 800 nm are attributed to the $d_{xz/yz} \rightarrow d_{x^2-y^2}$ and $d_{xy} \rightarrow d_{z^2}$ transitions, respectively. In contrast to **1**, the EPR spectra obtained for a frozen solution of **2** resemble the ones measured on the polycrystalline compound at 5.0 K (Figure S8). Particularly, we do not observe the reduction of the line width in the spectra obtained on the dissolved sample **2**. From this observation, we can conclude that not the g-strain but unresolved hyperfine interactions give indeed the main contribution to the observed anisotropic line broadening. Furthermore, the neglectable influence of intermolecular interactions is in line with our results from the Hirshfeld analysis (see Figures 6 and S9) and the evaluation of the χ^{-1} vs T plot (see Figure S5).

The solid-state EPR spectra of complexes **1** and **2** were simulated using the EasySpin-software,[30] and the simulation parameters are summarized in Table 2. In order to illustrate the influence of a finite H-strain parameter, an additional simulation with just isotropic broadening is given as gray lines in Figure 3 which clearly fails to reproduce the measured data shown as black lines.

https://doi.org/10.1021/acs.inorgchem.1c02881
Inorg. Chem. 2022, 61, 317−327

Table 2. Simulation Parameters Using the SH eq 1 Applied to the dc Magnetization, HF-EPR, and X-Band Data, Respectively, and Calculation Results

	1 (Co-SP)	2 (Co-TBP)
g_{HF-EPR}	1.99(2), 2.26(2), 2.34(2)	2.04(2), 2.06(2), 2.27(2)
g_{X-band}	2.01(3), 2.26(2), 2.34(2)	2.07(2), 2.05(2), 2.29(3)
ω_{X-band} (mT)	1.3(2)	2.5(3)
H-strain (MHz)[a]	250(30), 0, 0	0, 0, 750(50)
SOC constant (NEVPT2)	490.7 cm^{-1}	494.4 cm^{-1}
DFT (g-values)	2.01, 2.16, 2.20	2.06, 2.07, 2.19
NEVPT2 (g-values)	2.0, 2.28, 2.37	2,05, 2.06, 2.41

[a]The H-strain parameter describes the anisotropic line broadening due to unresolved hyperfine interactions.[30]

The application of high magnetic fields enables further resolution of the broad resonance lines. The magnetic field dependence of fixed powder spectra at T = 2 K is studied in the frequency regime between 50 and 300 GHz (black solid lines in Figure 4). For both **1** and **2**, the spectra exhibit two distinguishable resonance features which enable reading of the respective resonance fields and can be used to construct the frequency vs magnetic resonance field diagram (blue symbols in Figure 4). Expectedly, for low-spin Co(II) complexes, the resonance frequency obeys linear field dependence without a zero field splitting (ZFS) gap (blue solid lines in Figure 4). The data obtained at the respective highest frequencies, where the resolution of the anisotropic spectra is best, were fitted by using the SH eq 1 with an anisotropic g-factor. The resulting parameters were used to simulate the spectra measured at lower frequencies in order to demonstrate the consistency of the used model. The fit-results yield g(**1**) = [1.99(1), 2.26(1), 2.34(1)] and g(**2**) = [2.04(1), 2.06(1), 2.27(1)] which fully agree to the analyses of the X-band EPR data as shown in Table 2.

Magnetization Relaxation Dynamic Studies. Measurements of the ac susceptibility on **1** and **2** show the absence of an out-of-phase contribution to the dynamic susceptibility at zero magnetic dc field as expected for a spin S = 1/2 system. Field-induced slow magnetic relaxation behavior can however be observed for **1** when small external magnetic fields are applied as demonstrated by a peak in χ'' shown in Figure S10(c). Fitting the frequency-dependent χ'' data by a generalized Debye model (see eq S1) yields relaxation times τ up to 35 ms, while small eccentricities (α < 0.120(2) at 0.2 T and <0.185(3) at 1 T) indicate a single relaxation process with narrow distribution.

To find a proper model to evaluate the temperature-dependent relaxation times, the high and low temperature regions can be approximated separately by a linear fit shown as blue dashed lines in Figure 5. From the slope of these fits, the exponents of the participating relaxation processes in the respective temperature region can be estimated.[49] For our data, we find the temperature exponents of 1.9 and 1.6 in the low as well as 3.6 and 4.4 in the high temperature region for the data measured at 0.2 and 1 T, respectively. These values are close to the theoretical values of 1 and 5 for the direct process and a Raman process considering the involvement of multiplets with small but finite splitting induced, e.g., by hyperfine interactions.[50] Furthermore, there is no zero-field energy barrier for an S = 1/2 system, which is why we fit our data over the whole temperature range considering a direct process and a Raman process, only (eq 2).[50]

$$\tau^{-1} = AT + BT^{n} \quad (2)$$

While for a Raman relaxation process of a perfect Kramers doublet an exponent of n = 9 is expected, a much smaller value than 9 signifies the involvement of both acoustic and optical phonons in the Raman relaxation mechanism.[51]

For **2**, we also find a peak in χ'' signifying a slow relaxation of magnetization behavior. However, the observed relaxation times are much shorter (τ_{max} = 5 ms at 1 T), and the out-of-

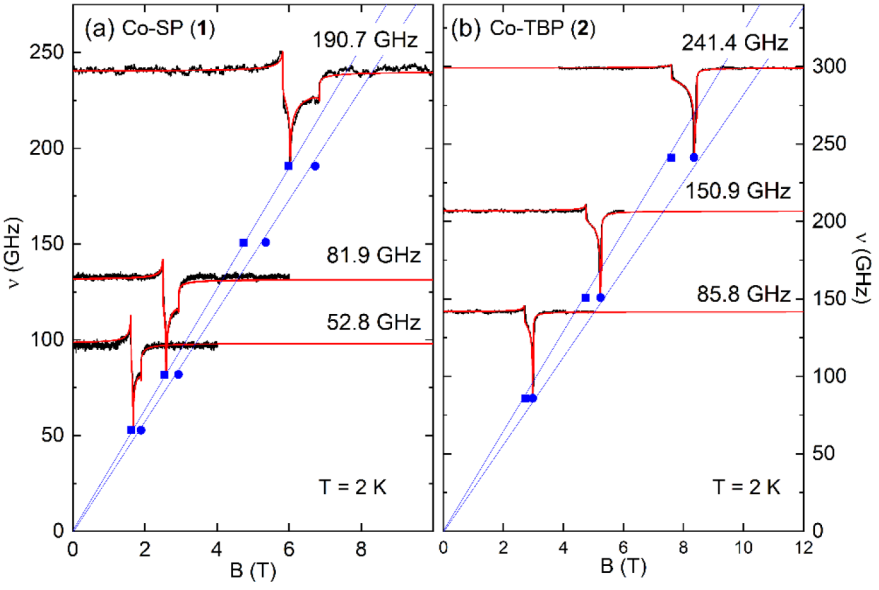

Figure 4. HF-EPR spectra measured at T = 2 K on fixed powder samples of **1** (a) and **2** (b) (black lines). The spectra are normalized and shifted by an offset of the respective measurement frequency which is indicated in the plot. Blue symbols show the resonance field positions of the respective resonance features which can be fitted by a linear fit without a ZFS gap (blue solid lines). Red solid lines correspond to a fit or simulation including an anisotropic g-factor as described in the main text.

https://doi.org/10.1021/acs.inorgchem.1c02881
Inorg. Chem. 2022, 61, 317−327

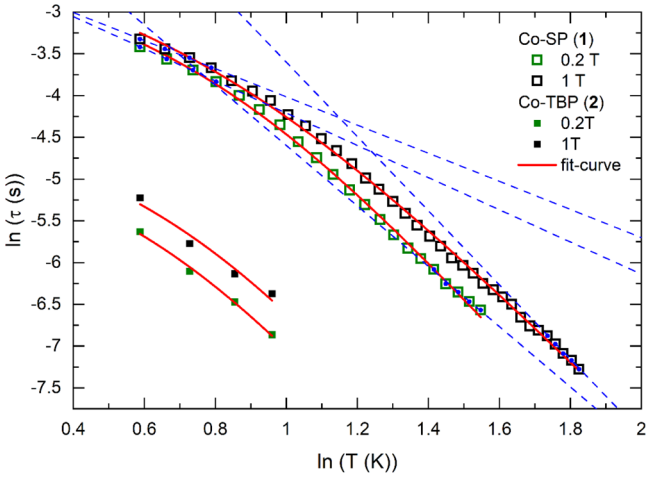

Figure 5. Temperature dependence of the relaxation time for **1** (open symbols) and **2** (filled symbols) in two different external magnetic fields. The data were collected by fitting the respective frequency dependence of χ'' by a generalized Debye model (see eq S1 and Figures S10 and S11). Dashed blue lines correspond to linear fits of the high and low temperature regions as described in the text, while solid red lines show a fit over the whole temperature range using eq 2. Blue dots mark the fit-range in correspondence to the linear fits.

phase signal is two orders smaller compared to **1** and only observable in the low temperature range (see Figure S11). Therefore, a detailed investigation of the involved relaxation processes is not possible. However, from a qualitative comparison, we can conclude that the magnetic relaxation time in complex **2** is significantly reduced compared to **1**. Furthermore, we fitted the data using eq 2 but with a fixed temperature exponent of 5 for the Raman relaxation term to avoid overparametrization. From this, we get an estimate for the prefactors of the direct and Raman relaxation terms. The evaluation of the corresponding fit-parameters shown in Table 3 reveals that this reduction in relaxation time is induced by an

Table 3. Parameters Obtained by the Fit of the Temperature Dependence of the Relaxation Times over the Whole Temperature Range Shown in Figure 5 Using eq 2 for an External Magnetic Field of 0.2 T/1 T

	A (s^{-1} K^{-1})	B (s^{-1} K^{-n})	n
1	11.6(8)/10.1(6)	0.5(3)/0.6(1)	4.7(10)/4.2(10)
2	96(30)/72(30)	6(4)/3(3)	5[a]/5[a]

[a]These values are fixed to avoid overparametrization of the fit.

increase of both the direct and the Raman relaxation terms. A fit using a direct term only failed to reproduce the data.

Observation of slow relaxation of magnetization in metal complexes possessing $S > 1/2$ is very common in the molecular magnetism research field. However, as already mentioned in an earlier section, the observation of slow relaxation of the magnetization in an $S = 1/2$ system is relatively scarce in the literature compared to the same phenomenon observed for $S > 1/2$ systems.[52−56] Reported examples for such complexes which show a finite out-of-phase susceptibility signal in the presence of an external magnetic field are, e.g., V(IV), Ni(I), Ni(III), Mn(IV), Cu(II), Fe(III), and Co(II) complexes.[16,17,19,21,24,57] In ref 57, it is shown that the unquenched orbital contribution to the magnetic moment of the two-coordinate Ni(I) is the origin of field-induced slow relaxation of magnetization in these complexes. In the Co(II) complexes studied at hand, strong spin−orbit coupling is clearly evident from our X-band and HF-EPR investigations performed on **1** and **2** which show large g-factors (compared to $g = 2.0023$) and an anisotropic g-value. It is also confirmed by our numerical studies (see Table 2). The calculated spin−orbit coupling (SOC) constant is large but only marginally differs between **1** and **2** (see Table 2). Hence, while, in general, the appearance of slow relaxation of the magnetization behavior can be explained by the strong SOC in both complexes, the observed clear differences in the relaxation times must have another origin, i.e., the driving mechanism suppressing the relaxation time in **2** compared to **1** is to be identified.[24]

One candidate to cause the different relaxation times in both complexes is hyperfine interactions. Our simulations of the X-band EPR data strongly imply finite hyperfine interactions in both complexes as evidenced by the anisotropic line broadening which is reflected by the H-strain parameter. Even though due to lack of resolution, no quantitative number for the strength of the hyperfine interaction can be given, the H-strain parameter for **2** appears to be significantly larger than for **1**. We conclude that also the hyperfine interaction is larger in **2** than in **1** and thereby could drive faster relaxation. However, on an absolute scale, the difference in the observed H-strain parameter is only 500 MHz (0.017 cm^{-1}), and the overall HF interaction strength seems to be too weak to resolve any HF features in the X-band EPR spectra. Hence, we conclude that the HF interaction may not be the driving mechanism to explain the significant differences in relaxation behavior of the investigated compounds. Instead, we assume that the dissimilar g-anisotropies induced by the geometrical arrangement of the surrounding ligand might be the most reasonable explanation for the observed magnetic relaxation behavior.

We also would like to mention here the scenario considering intermolecular dipolar interactions.[24] Indeed, the distance between nearest neighboring Co(II) ions in **2** amounts to 9.81 Å which is slightly smaller than the minimal distance in **1** (10.68 Å). This results in different dipolar interaction strengths of 2.7 and 2.1 MHz in **2** and **1**, respectively. However, comparisons to literature results imply that these small deviations in minimal Co(II)···Co(II) distances cannot account for the strong difference in relaxation behavior.[19] This is in line with our experimental findings on a frozen solution sample described in the previous section. However, since intermolecular coupling pathways are a sensitive issue in order to evaluate magnetic relaxation processes, a Hirshfeld surface analysis and DFT calculations were applied to investigate the nature and strength of possible intermolecular interactions (see the following sections).

Hirshfeld Surface Analysis of Co-SP (1) and Co-TBP (2). In order to analyze the inter- and intramolecular interactions observed in the solid state, a Hirshfeld surface analysis was carried out on the cation moieties of both complexes (Figure 6). The various regions of color on these surfaces describe the inter- and intramolecular contacts present in their crystal structures. Two-dimensional (2D) fingerprint plots (Figure S9) were also generated for the cations of both complexes and used to visualize supramolecular features such as weak inter- and intramolecular interactions and close contacts as seen in their crystal structures. Both the Hirshfeld surface and fingerprint plots were extracted from the d_i and d_e values using *CrystalExplorer*.[58] d_i represents the distance from the Hirshfeld surface to the nearest atom inside the surface

https://doi.org/10.1021/acs.inorgchem.1c02881
Inorg. Chem. 2022, 61, 317−327

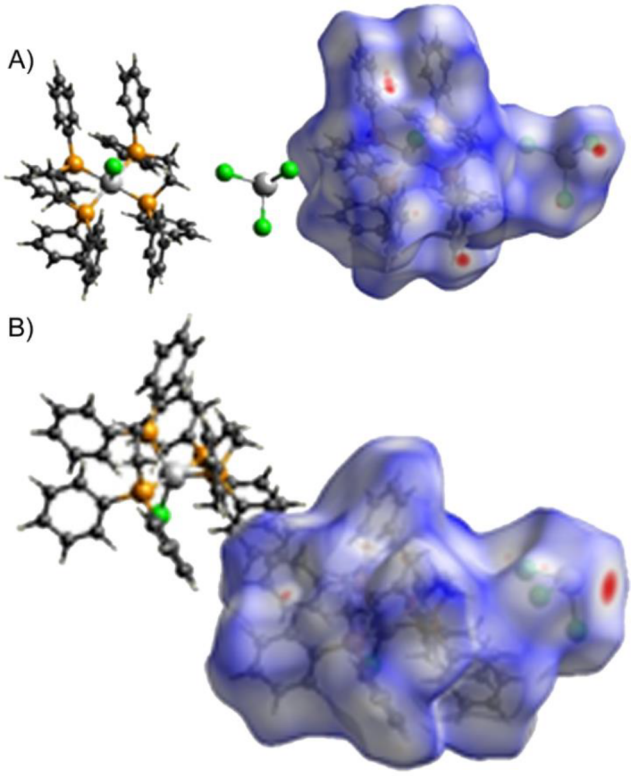

Figure 6. Hirshfeld surface analysis mapped with d_{norm} and showing two adjacent molecules outside the surface for the cations in complex **1** (A) and complex **2** (B). The red colors indicate contacts with distances shorter than the van der Waals radii and indicate very weak inter- or intramolecular interactions.

with d_e being the distance from the nearest atom outside the surface.[59] The results of these plots indicate that the percentage of intermolecular H···H contacts is 55.8% in **1** and 54.3% in **2** of the total share. The other significant contributions including reciprocal contacts are Cl···H, C···H, Sn···H, and C···C having relative contributions of 22.4, 14.4, 5.3, and 1.3% in **1** and 20.2, 17.8, 5.3, and 1.3% in **2**, respectively. These values and the absence of sharp spikes in the fingerprint plots support the notion that all of the inter- and intramolecular interactions in the cations of both complexes are relativity weak in support of no classical hydrogen bonds being observed in their crystal structures.

Theoretical Calculations. To estimate the intermolecular coupling strength J between two neighboring Co(II) ions, we have taken a dimeric unit from the crystal packing with the Co(II)···Co(II) having the shortest intermolecular distance (This is found to be 9.81 for **1** and 10.68 Å for **2**.). DFT calculations yield J values of −0.01 and 0.0 cm^{-1}, respectively, for complexes **1** and **2** (see Figure S12). These values imply that there are no strong intermolecular interactions that could rationalize the observation of slow relaxation of magnetization. Thus, we conclude that the observed relaxation behavior is mainly influenced by the g-anisotropy of the ground state.

DFT geometry optimization for high- (HS) and low-spin (LS) configuration suggests a low-spin state as ground state in both complexes, and the first excited quartet state in **1** and **2** is found to be at 29.4 and 43.7 kJ/mol higher energy from the ground state, respectively. For complex **1**, the computed bond lengths of the Co(II)−P_{avg} and Co(II)−Cl are found to be 2.539/2.353 and 2.337/2.341 Å, respectively, for HS/LS. Likewise, the computed bond lengths of the Co(II)−P_{avg} and Co−Cl amount to 2.519/2.335 and 2.339/2.491 Å for HS/LS in complex **2**. The computed structural parameters of the low-spin state geometry are in good agreement with the single-crystal X-ray structural data, as shown in Figure 7. The

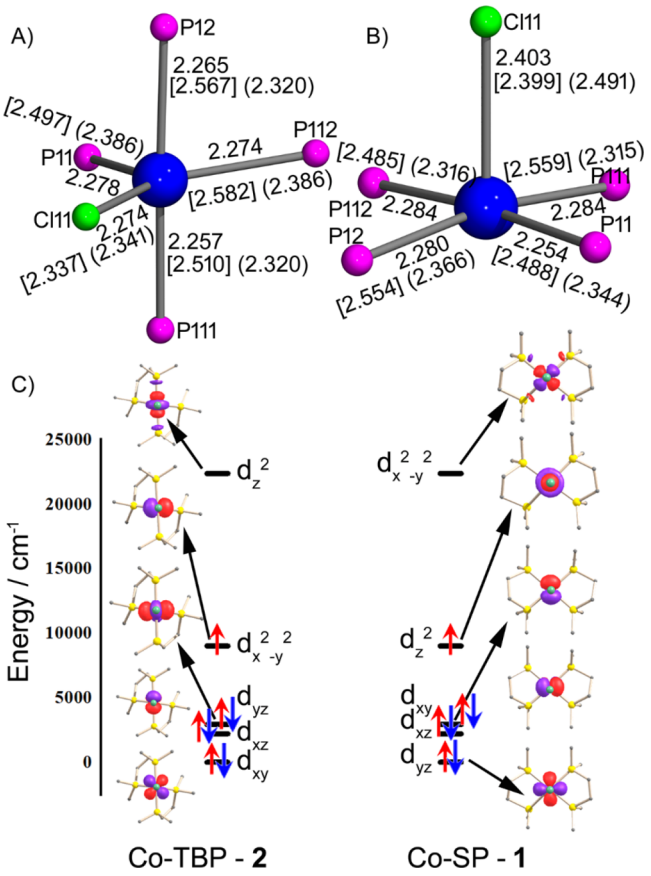

Figure 7. Bond lengths (in Å) observed for the optimized structure of high-spin (square bracket) and low-spin (curved bracket) complexes **2** (panel A) and **1** (panel B) which are compared with the bond length (in Å) observed in the X-ray structure. In (C), the eigenvalue plots of complexes Co-SP (**1**) and Co-TBP (**2**) based on the *ab initio* Ligand Field Theory (AI-LFT) are shown.

computed energetics from the calculations are consistent with magnetic data and HF-EPR measurements. The g-values obtained from NEVPT2 calculations reproduce almost perfectly the experimental g-anisotropy observed (see Table 2), offering confidence in the chosen methodology. The average g-anisotropy for **1** and **2** is estimated to be 2.173 and 2.216, respectively, i.e., a slightly larger g-anisotropy is found in complex **2** compared to **1** which is also reflected in the HF-EPR or X-band EPR data. The computed spin−orbit coupling constants for both complexes are found to be similar (490.7 and 494.4 cm^{-1} for **1** and **2**, respectively), and therefore, the anisotropic g arises from the difference in the electronic structure and coordination geometry around the Co(II) ions. The eigenvalue plot (see Figure 7) reveals that the highest single occupied molecular orbital (SOMO) for **1** is d_{z^2}, while for complex **2**, it is the $d_{x^2-y^2}$ orbital which is essentially due to the observed geometric difference.

https://doi.org/10.1021/acs.inorgchem.1c02881
Inorg. Chem. 2022, 61, 317−327

CONCLUSION

The synthetic approach followed led us to isolate the two different geometric isomers, namely square pyramidal (Co-SP (**1**)) and trigonal bipyramidal (Co-TBP (**2**)) five-coordinate Co(II) complexes with the general molecular formula of $[Co(DPPE)_2Cl]SnCl_3$. Detailed dc magnetic susceptibility measurements performed on polycrystalline samples of **1** and **2** disclose that the Co(II) ions in both complexes are stabilized in the low-spin $S = 1/2$ state. This is in good agreement with the energetics computed for **1** and **2** through DFT calculations, which predict that the low-spin state for both complexes is lower in energy than the corresponding high-spin state. The predicted coordination geometry-assisted change in the electronic properties of the low-spin Co(II) ions was experimentally proven by X-band and HF-EPR measurements. Observation of slow relaxation of magnetization for undiluted complexes with $S = 1/2$ has been observed in both, **1** and **2**. The relaxation time extracted for **1** is significantly larger than for **2**. Proven that the intermolecular interaction in both complexes is extremely weak or nil (through frozen solution X-band EPR, X-ray analysis, Hirshfeld surface analysis, and DFT calculations) and considering the similar spin−orbit coupling constant computed for both complexes, the experimentally observed distinct relaxation behaviors of these complexes are attributed to changes in g-anisotropy. Irrefutably, this anisotropy strongly depends on the spatial arrangement of the ligands around the Co(II) ions, i.e., the coordination geometry. Nevertheless, the relaxation times extracted for the complexes at hand are larger than those of comparable undiluted low-spin Co(II) systems.[19] Therefore, both complexes **1** and **2** are envisaged as a potential molecular qubit system with long phase memory times. The findings reported in this article will certainly pave the way to construct a new generation of Co(II) complexes in different geometries with exceptional magnetic properties.

ASSOCIATED CONTENT

Supporting Information

The Supporting Information is available free of charge at https://pubs.acs.org/doi/10.1021/acs.inorgchem.1c02881.

IR, UV−vis, and PXRD spectra for all complexes, packing diagrams, supporting dc and ac magnetic data, X-band EPR spectra for diluted samples, fingerprint plots from Hirshfeld surface analysis, and computed spin density plots (PDF)

Accession Codes

CCDC 2080078−2080079 contain the supplementary crystallographic data for this paper. These data can be obtained free of charge via www.ccdc.cam.ac.uk/data_request/cif, or by emailing data_request@ccdc.cam.ac.uk, or by contacting The Cambridge Crystallographic Data Centre, 12 Union Road, Cambridge CB2 1EZ, UK; fax: +44 1223 336033.

AUTHOR INFORMATION

Corresponding Authors

Lena Spillecke − *Kirchhoff Institute for Physics, Heidelberg University, 69120 Heidelberg, Germany*; orcid.org/0000-0003-0163-6783; Email: lena.spillecke@kip.uni-heidelberg.de

Rüdiger Klingeler − *Kirchhoff Institute for Physics and Center for Advanced Materials, Heidelberg University, 69120 Heidelberg, Germany*; Email: ruediger.klingeler@kip.uniheidelberg.de

Maheswaran Shanmugam − *Department of Chemistry, Indian Institute of Technology Bombay, Mumbai 400076, India*; Email: eswar@chem.iitb.ac.in

Gopalan Rajaraman − *Department of Chemistry, Indian Institute of Technology Bombay, Mumbai 400076, India*; orcid.org/0000-0001-6133-3026; Email: rajaraman@chem.iitb.ac.in

Authors

Shalini Tripathi − *Department of Chemistry, Indian Institute of Technology Bombay, Mumbai 400076, India*

Changhyun Koo − *Kirchhoff Institute for Physics, Heidelberg University, 69120 Heidelberg, Germany*

Arne Bahr − *Kirchhoff Institute for Physics, Heidelberg University, 69120 Heidelberg, Germany*

Abinash Swain − *Department of Chemistry, Indian Institute of Technology Bombay, Mumbai 400076, India*

Rajashi Haldar − *Department of Chemistry, Indian Institute of Technology Bombay, Mumbai 400076, India*

Mursaleem Ansari − *Department of Chemistry, Indian Institute of Technology Bombay, Mumbai 400076, India*

Jerry Jasinski − *Department of Chemistry, Keene State College, Keene, New Hampshire 03435-2001, United States*

Complete contact information is available at: https://pubs.acs.org/10.1021/acs.inorgchem.1c02881

Author Contributions

⊥L.S. and S.T. contributed equally.

Notes

The authors declare no competing financial interest.

ACKNOWLEDGMENTS

Funding by Bundesministerium für Forschung und Bildung via project *SpinFun* (13XP5088) and by Deutsche Forschungsgemeinschaft (DFG) under Germany's Excellence Strategy EXC2181/1-390900948 (the Heidelberg STRUCTURES Excellence Cluster) is gratefully acknowledged. L.S. acknowledges support by Landesgradiertenförderung via the research training group *Basic building blocks for quantum enabled technologies*, and C.K. acknowledges support by DFG project KO5480/1-1. M.S. acknowledges various funding agencies namely SERB (CRG/2019/004185 and SPR/2019/001145), CSIR (01(2933)/18/EMR-II), and IIT Bombay for the financial support. Special thanks to IRCC, IIT Bombay-EPR central facility, for the support and assistance. G.R. would like to thank DST/SERB (CRG/2018/000430, DST/SJF/CSA03/2018-10; SB/SJF/2019-20/12; SPR/2019/001145) for financial support. We would like to extend our sincere thanks to Prof. Markus Enders and Dr. Hubert Wadepohl for providing lab facilities and resources to synthesize the samples and providing their valuable suggestions to A.S.

REFERENCES

(1) Christou, G.; Gatteschi, D.; Hendrickson, D. N.; Sessoli, R. Single-Molecule Magnets. *MRS Bull.* **2000**, *25* (11), 66−71.

(2) Sessoli, R.; Gatteschi, D.; Caneschi, A.; Novak, M. A. Magnetic bistability in a metal-ion cluster. *Nature* **1993**, *365* (6442), 141−143.

(3) Yang, J.; Wang, Y.; Wang, Z.; Rong, X.; Duan, C.-K.; Su, J.-H.; Du, J. Observing Quantum Oscillation of Ground States in Single Molecular Magnet. *Phys. Rev. Lett.* **2012**, *108* (23), 230501.

(4) Tesi, L.; Lucaccini, E.; Cimatti, I.; Perfetti, M.; Mannini, M.; Atzori, M.; Morra, E.; Chiesa, M.; Caneschi, A.; Sorace, L.; Sessoli, R. Quantum coherence in a processable vanadyl complex: new tools for the search of molecular spin qubits. *Chemical Science* **2016**, *7* (3), 2074−2083.
(5) Bar, A. K.; Pichon, C.; Sutter, J.-P. Magnetic anisotropy in two- to eight-coordinated transition−metal complexes: Recent developments in molecular magnetism. *Coord. Chem. Rev.* **2016**, *308*, 346−380.
(6) Kajiwara, T.; Takahashi, K.; Hiraizumi, T.; Takaishi, S.; Yamashita, M. Structural correlations between the crystal field and magnetic anisotropy of Ln−Cu single-molecule magnets. *CrystEngComm* **2009**, *11* (10), 2110−2116.
(7) Harriman, K L. M.; Jesse, M.; Elizaveta, A. S.; Skye, F.; Muralee, M. *See-Saw Shaped Dy(III) Single-Molecule Magnets with High Anisotropy Barriers*. 2020, https://chemrxiv.org/engage/chemrxiv/article-details/60c7477af96a00af53286f1e (accessed 2021-12-14), DOI: 10.26434/chemrxiv.11673927.v1.
(8) Langley, S. K.; Chilton, N. F.; Moubaraki, B.; Murray, K. S. Anisotropy barrier enhancement via ligand substitution in tetranuclear {CoIII2LnIII2} single molecule magnets. *Chem. Commun.* **2013**, *49* (62), 6965−6967.
(9) Palacios, M. A.; Nehrkorn, J.; Suturina, E. A.; Ruiz, E.; Gómez-Coca, S.; Holldack, K.; Schnegg, A.; Krzystek, J.; Moreno, J. M.; Colacio, E. Analysis of Magnetic Anisotropy and the Role of Magnetic Dilution in Triggering Single-Molecule Magnet (SMM) Behavior in a Family of CoIIYIII Dinuclear Complexes with Easy-Plane Anisotropy. *Chem. - Eur. J.* **2017**, *23* (48), 11649−11661.
(10) Perfetti, M.; Rinck, J.; Cucinotta, G.; Anson, C. E.; Gong, X.; Ungur, L.; Chibotaru, L.; Boulon, M.-E.; Powell, A. K.; Sessoli, R. Single Crystal Investigations Unravel the Magnetic Anisotropy of the "Square-In Square" Cr4Dy4 SMM Coordination Cluster. *Front. Chem.* **2019**, *7*, 6.
(11) Bazhenova, T. A.; Zorina, L. V.; Simonov, S. V.; Mironov, V. S.; Maximova, O. V.; Spillecke, L.; Koo, C.; Klingeler, R.; Manakin, Y. V.; Vasiliev, A. N.; Yagubskii, E. B. The first pentagonal-bipyramidal vanadium(iii) complexes with a Schiff-base N3O2 pentadentate ligand: synthesis, structure and magnetic properties. *Dalton Transactions* **2020**, *49* (43), 15287−15298.
(12) Escalera-Moreno, L.; Baldoví, J. J.; Gaita-Ariño, A.; Coronado, E. Spin states, vibrations and spin relaxation in molecular nanomagnets and spin qubits: a critical perspective. *Chemical Science* **2018**, *9* (13), 3265−3275.
(13) Martínez-Pérez, M. J.; Cardona-Serra, S.; Schlegel, C.; Moro, F.; Alonso, P. J.; Prima-García, H.; Clemente-Juan, J. M.; Evangelisti, M.; Gaita-Ariño, A.; Sesé, J.; van Slageren, J.; Coronado, E.; Luis, F. Gd-Based Single-Ion Magnets with Tunable Magnetic Anisotropy: Molecular Design of Spin Qubits. *Phys. Rev. Lett.* **2012**, *108* (24), 247213.
(14) Yu, C.-J.; Graham, M. J.; Zadrozny, J. M.; Niklas, J.; Krzyaniak, M. D.; Wasielewski, M. R.; Poluektov, O. G.; Freedman, D. E. Long Coherence Times in Nuclear Spin-Free Vanadyl Qubits. *J. Am. Chem. Soc.* **2016**, *138* (44), 14678−14685.
(15) Xu, M.-X.; Liu, Z.; Dong, B.-W.; Cui, H.-H.; Wang, Y.-X.; Su, J.; Wang, Z.; Song, Y.; Chen, X.-T.; Jiang, S.-D.; Gao, S. Single-Crystal Study of a Low Spin Co(II) Molecular Qubit: Observation of Anisotropic Rabi Cycles. *Inorg. Chem.* **2019**, *58* (4), 2330−2335.
(16) Atzori, M.; Tesi, L.; Morra, E.; Chiesa, M.; Sorace, L.; Sessoli, R. Room-Temperature Quantum Coherence and Rabi Oscillations in Vanadyl Phthalocyanine: Toward Multifunctional Molecular Spin Qubits. *J. Am. Chem. Soc.* **2016**, *138* (7), 2154−2157.
(17) Boča, R.; Rajnák, C.; Titiš, J.; Valigura, D. Field Supported Slow Magnetic Relaxation in a Mononuclear Cu(II) Complex. *Inorg. Chem.* **2017**, *56* (3), 1478−1482.
(18) Ding, M.; Cutsail Iii, G. E.; Aravena, D.; Amoza, M.; Rouzières, M.; Dechambenoit, P.; Losovyj, Y.; Pink, M.; Ruiz, E.; Clérac, R.; Smith, J. M. A low spin manganese(iv) nitride single molecule magnet. *Chemical Science* **2016**, *7* (9), 6132−6140.
(19) Cui, H.-H.; Wang, J.; Chen, X.-T.; Xue, Z.-L. Slow magnetic relaxation in five-coordinate spin-crossover cobalt(ii) complexes. *Chem. Commun.* **2017**, *53* (67), 9304−9307.
(20) Zadrozny, J. M.; Gallagher, A. T.; Harris, T. D.; Freedman, D. E. A Porous Array of Clock Qubits. *J. Am. Chem. Soc.* **2017**, *139* (20), 7089−7094.
(21) Buades, A. B.; Arderiu, V. S.; Maxwell, L.; Amoza, M.; Choquesillo-Lazarte, D.; Aliaga-Alcalde, N.; Viñas, C.; Teixidor, F.; Ruiz, E. Slow-spin relaxation of a low-spin S = 1/2 FeIII carborane complex. *Chem. Commun.* **2019**, *55* (26), 3825−3828.
(22) Bhowmick, I.; Shaffer, D. W.; Yang, J. Y.; Shores, M. P. Single molecule magnet behaviour in a square planar S = 1/2 Co(ii) complex and spin-state assignment of multiple relaxation modes. *Chem. Commun.* **2020**, *56* (49), 6711−6714.
(23) Chen, L.; Song, J.; Zhao, W.; Yi, G.; Zhou, Z.; Yuan, A.; Song, Y.; Wang, Z.; Ouyang, Z.-W. A mononuclear five-coordinate Co(ii) single molecule magnet with a spin crossover between the S = 1/2 and 3/2 states. *Dalton Transactions* **2018**, *47* (46), 16596−16602.
(24) Bhowmick, I.; Roehl, A. J.; Neilson, J. R.; Rappé, A. K.; Shores, M. P. Slow magnetic relaxation in octahedral low-spin Ni(iii) complexes. *Chemical Science* **2018**, *9* (31), 6564−6571.
(25) Stalick, J. K.; Corfield, P. W. R.; Meek, D. W. Structural isomerization and rapid interconversion of two five-coordinate cobalt(II) complexes containing chelating diphosphine ligands. *J. Am. Chem. Soc.* **1972**, *94* (17), 6194−6196.
(26) Stalick, J. K.; Meek, D. W.; Ho, B. Y. K.; Zuckerman, J. J. 119mSn Mössbauer parameters and crystal structure of the SnCl3− ion in two forms of chlorobis[bis-(1,2-diphenylphosphino)ethane]-cobalt(II) trichlorostannate(II). *J. Chem. Soc., Chem. Commun.* **1972**, *0* (11), 630−632.
(27) Stalick, J. K.; Corfields, P. W. R.; Meek, D. W. Trigonal-bipyramidal and square-pyramidal five-coordinate cobalt(II). Crystal and molecular structures of the red and green isomers of chlorobis[1,2-bis(diphenylphosphino)ethane]cobalt(II) trichlorostannate(II). *Inorg. Chem.* **1973**, *12* (7), 1668−1675.
(28) Sheldrick, G. M. Crystal structure refinement withSHELXL. *Acta Crystallogr., Sect. C: Struct. Chem.* **2015**, *71* (1), 3−8.
(29) Comba, P.; Großhauser, M.; Klingeler, R.; Koo, C.; Lan, Y.; Müller, D.; Park, J.; Powell, A.; Riley, M. J.; Wadepohl, H. Magnetic Interactions in a Series of Homodinuclear Lanthanide Complexes. *Inorg. Chem.* **2015**, *54* (23), 11247−11258.
(30) Stoll, S.; Schweiger, A. EasySpin, a comprehensive software package for spectral simulation and analysis in EPR. *J. Magn. Reson.* **2006**, *178* (1), 42−55.
(31) Frisch, J. M. *GAUSSIAM 09 (Revision 02)*; Gaussian Inc.: Wallingford, CT, 2009.
(32) Grimme, S. *J. Comput. Chem.* **2006**, *27*, 1787−1799.
(33) Hay, P. J.; Wadt, W. R. Ab initio effective core potentials for molecular calculations. Potentials for the transition metal atoms Sc to Hg. *J. Chem. Phys.* **1985**, *82* (1), 270−283.
(34) Hehre, W. J.; Ditchfield, R.; Pople, J. A. Self—Consistent Molecular Orbital Methods. XII. Further Extensions of Gaussian—Type Basis Sets for Use in Molecular Orbital Studies of Organic Molecules. *J. Chem. Phys.* **1972**, *56* (5), 2257−2261.
(35) Neese, F. The ORCA program system. *Wiley Interdiscip. Rev.: Comput. Mol. Sci.* **2012**, *2* (1), 73−78.
(36) van Lenthe, E.; van der Avoird, A.; Wormer, P. E. S. Density functional calculations of molecular hyperfine interactions in the zero order regular approximation for relativistic effects. *J. Chem. Phys.* **1998**, *108* (12), 4783−4796.
(37) van Lenthe, E.; Baerends, E. J.; Snijders, J. G. Relativistic regular two-component Hamiltonians. *J. Chem. Phys.* **1993**, *99* (6), 4597−4610.
(38) Schaefer, A.; Horn, H.; Ahlrichs, R. Fully optimized contracted Gaussian basis sets for atoms lithium to krypton. *J. Chem. Phys.* **1992**, *97* (4), 2571−7.
(39) Weigend, F.; Ahlrichs, R. Balanced basis sets of split valence, triple zeta valence and quadruple zeta valence quality for H to Rn:

Design and assessment of accuracy. *Phys. Chem. Chem. Phys.* **2005**, *7* (18), 3297−3305.
(40) Ruamps, R.; Maurice, R.; Batchelor, L.; Boggio-Pasqua, M.; Guillot, R.; Barra, A. L.; Liu, J.; Bendeif, E.-E.; Pillet, S.; Hill, S.; Mallah, T.; Guihéry, N. Giant Ising-Type Magnetic Anisotropy in Trigonal Bipyramidal Ni(II) Complexes: Experiment and Theory. *J. Am. Chem. Soc.* **2013**, *135* (8), 3017−3026.
(41) Maurice, R.; Bastardis, R.; Graaf, C. d.; Suaud, N.; Mallah, T.; Guihéry, N. Universal Theoretical Approach to Extract Anisotropic Spin Hamiltonians. *J. Chem. Theory Comput.* **2009**, *5* (11), 2977−2984.
(42) Brown, I. D. 14 - The Bond-Valence Method: An Empirical Approach to Chemical Structure and Bonding. In *Industrial Chemistry Library*; O'Keeffe, M., Navrotsky, A., Eds.; Elsevier: 1981; Vol. *2*, pp 1−30.
(43) Pinsky, M.; Avnir, D. Continuous Symmetry Measures. 5. The Classical Polyhedra. *Inorg. Chem.* **1998**, *37* (21), 5575−5582.
(44) Addison, A. W.; Rao, T. N.; Reedijk, J.; van Rijn, J.; Verschoor, G. C. Synthesis, structure, and spectroscopic properties of copper(II) compounds containing nitrogen−sulphur donor ligands; the crystal and molecular structure of aqua[1,7-bis(N-methylbenzimidazol-2′-yl)-2,6-dithiaheptane]copper(II) perchlorate. *J. Chem. Soc., Dalton Trans.* **1984**, *7*, 1349−1356.
(45) Malatesta, V.; McGarvey, B. R. Single Crystal Electron Spin Resonance Of Low Spin Co(II) And Of Cu(II) Schiff Base Complexes. *Can. J. Chem.* **1975**, *53* (24), 3791−3800.
(46) Sethulakshmi, C. N.; Manoharan, P. T. EPR and electronic structural investigations of a few low-spin bis(tertiary phosphine) complexes of cobalt(II). *Inorg. Chem.* **1981**, *20* (8), 2533−2539.
(47) von Zelewsky, A.; Zobrist, M. EPR. Spectroscopic Investigations of Planar Cu (II)- and Low-Spin Co (II)-Complexes in Nematic Phases and in Single Crystals. *Helv. Chim. Acta* **1981**, *64* (7), 2154−2161.
(48) Jenkins, D. M.; Di Bilio, A. J.; Allen, M. J.; Betley, T. A.; Peters, J. C. Elucidation of a Low Spin Cobalt(II) System in a Distorted Tetrahedral Geometry. *J. Am. Chem. Soc.* **2002**, *124* (51), 15336−15350.
(49) Rajnák, C.; Boča, R. Reciprocating thermal behavior in the family of single ion magnets. *Coord. Chem. Rev.* **2021**, *436*, 213808.
(50) Abragam, A.; Bleaney, B. *Electron paramagnetic resonance of transition ions*; OUP Oxford: 2012.
(51) Shrivastava, K. N. Theory of Spin−Lattice Relaxation. *Phys. Status Solidi B* **1983**, *117* (2), 437−458.
(52) Świtlicka, A.; Machura, B.; Penkala, M.; Bieńko, A.; Bieńko, D. C.; Titiš, J.; Rajnák, C.; Boča, R.; Ozarowski, A. Slow magnetic relaxation in hexacoordinated cobalt(ii) field-induced single-ion magnets. *Inorg. Chem. Front.* **2020**, *7* (14), 2637−2650.
(53) Nemec, I.; Herchel, R.; Trávníček, Z. Suppressing of slow magnetic relaxation in tetracoordinate Co(II) field-induced single-molecule magnet in hybrid material with ferromagnetic barium ferrite. *Sci. Rep.* **2015**, *5* (1), 10761.
(54) Sertphon, D.; Murray, K. S.; Phonsri, W.; Jover, J.; Ruiz, E.; Telfer, S. G.; Alkaş, A.; Harding, P.; Harding, D. J. Slow relaxation of magnetization in a bis-mer-tridentate octahedral Co(ii) complex. *Dalton Transactions* **2018**, *47* (3), 859−867.
(55) Cieslik, P.; Comba, P.; Hergett, W.; Klingeler, R.; Plny, G. F. P.; Spillecke, L.; Velmurugan, G. Molecular magnetic properties of a dysprosium(III) complex coordinated to a nonadentate bispidine ligand. *Z. Anorg. Allg. Chem.* **2021**, *647* (8), 843−849.
(56) Mitsuhashi, R.; Hosoya, S.; Suzuki, T.; Sunatsuki, Y.; Sakiyama, H.; Mikuriya, M. Zero-field slow relaxation of magnetization in cobalt(ii) single-ion magnets: suppression of quantum tunneling of magnetization by tailoring the intermolecular magnetic coupling. *RSC Adv.* **2020**, *10* (71), 43472−43479.
(57) Poulten, R. C.; Page, M. J.; Algarra, A. G.; Le Roy, J. J.; López, I.; Carter, E.; Llobet, A.; Macgregor, S. A.; Mahon, M. F.; Murphy, D. M.; Murugesu, M.; Whittlesey, M. K. Synthesis, Electronic Structure, and Magnetism of [Ni(6-Mes)2]+: A Two-Coordinate Nickel(I) Complex Stabilized by Bulky N-Heterocyclic Carbenes. *J. Am. Chem. Soc.* **2013**, *135* (37), 13640−13643.
(58) *Crystal Explorer 17*; University of Western Australia. http://crystalexplorer.scb.uwa.edu.au/ (accessed 2021-12-14).
(59) Wolff, K. S.; Grimwood, J. D.; McKinnon, J. J.; Turner, J. M.; Jayatilaka, D.; Spackman, M. A. *CrystalExplorer (Version 3.1)*; University of Australia: 2012.

https://doi.org/10.1021/acs.inorgchem.1c02881
Inorg. Chem. 2022, 61, 317−327